Article

Nanostructuring of SnO_2 thin films by associating glancing angle deposition and sputtering pressure for gas sensing applications

Achraf El Mohajir [1], Mohammad Arab Pour Yazdi [2,3], Anna Krystianiak [4], Olivier Heintz [4], Nicolas Martin [1], Franck Berger [1] and Jean-Baptiste Sanchez [1,*]

[1] Institut FEMTO-ST, UMR 6174, CNRS, Univ. Bourgogne Franche-Comté, 15B, Avenue des Montboucons, 25030 Besançon, France; achraf.elmohajir@femto-st.fr (A.E.M.); nicolas.martin@femto-st.fr (N.M.) ; franck.berger@univ-fcomte.fr (F.B.) ; jbsanche@femto-st.fr (J.B.S)
[2] Institut FEMTO-ST, UMR 6174, CNRS, Univ. Bourgogne Franche-Comté, UTBM, Site de Montbéliard, 90010 Belfort, France; mohammad.arab-pour-yazdi@utbm.fr (M.A.P.Y)
[3] Anton Paar TriTec SA, Les Vernets 6, 2035 Corcelles, Switzerland, https://www.anton-paar.com
[4] Laboratoire ICB, UMR 6303 CNRS, Univ. Bourgogne Franche-Comté, 9, Avenue Alain Savary, BP 47 870, 21078 Dijon Cedex, France; anna.krystianiak@u-bourgogne.fr (A.K); olivier.heintz@u-bourgogne.fr (O.H.);
* Correspondence: jbsanche@femto-st.fr (J.B.S.)

Abstract: SnO_2 thin films were prepared by conventional and GLancing Angle Deposition reactive sputtering and their gas sensing properties were investigated. The porosity of the as-prepared films has been widely assessed using optical methods and sensing performances of these active layers were correlated with the evolution of surface and films' porosity as a function of deposition conditions and annealing treatment. The sensor made of inclined columns grown at high sputtering pressure (6.10^{-3} mbar) and annealed at 500°C in air exhibited the best response to benzene with a limit of detection of 30 ppb. In addition, successful BTEX (*i.e.*, benzene, toluene, ethylbenzene, and xylenes) discrimination was achieved by combining the sensing signals of 4 nanostructured tin oxide-based gas sensors.

Keywords: GLAD; SnO_2; nano-columns; BTEX gas sensor; porous architecture

1. Introduction

Metal oxide semiconductor (MOS) gas sensors are the dominant gas sensing devices for monitoring the presence of air pollutants [1,2]. Despite a poor selectivity, these chemical gas sensors show many advantages such as low cost, flexibility of production, reduced power consumption as well as high sensitivity and minimal performance drift over time in controlled atmosphere (laboratory conditions). The sensing performances of these metal oxide-based gas sensor are directly controlled by the grain size and the morphology of the sensing materials [3–8]. In order to improve MOS gas sensor performances, most studies have been focused on structuring of sensitive thin films. In particular, the nanostructuring of the sensitive material led to an improvement in detection performance, especially to reach very low detection limits in the ppb level or lower. Several innovative fabrication methods have been developed to produce high sensitive chemical gas sensors with metal oxide nanostructures including bottom-up (chemical vapor deposition (CVD), sol-gel processes, thermal evaporation, hydrothermal route, reactive sputtering) and also top-down approaches (electron-beam lithography, reactive ion etching, field-ion beam technology) [9–14]. Recently, the GLancing Angle Deposition method (GLAD) has been applied in reactive sputtering for the growth of different nano-sized columnar films with controlled porosities and shapes [15–17]. Thin films with very original architectures such

as normal and inclined columns, zigzag or spiral structures can be achieved with this deposition method [18–20]. Although GLAD technique offers a fully three-dimensional control of the films and almost no limitation on materials that can be fabricated, only a few studies address the use of GLAD deposition technique for the development of sensitive layers for chemical gas sensor applications. Nevertheless, we can cite works concerning the use of copper oxide films [21], ZnO nanospiral thin films [22], nanocolumnar SnO_2 and NiO metal oxides [23] or more recently a sensor array composed of different nanocolumnar structures made of metal oxides [24]. All these studies have shown that the interaction mechanisms between gas phase and metal oxide are fully dependent on the open porous microstructure associated with GLAD films. Thus, to fabricate efficient gas sensor, it is interesting to produce materials with a large surface in contact with the gas phase as target analytes can easily interact with the high surface area microstructure of thin films.

In this study, GLAD method has been used to produce tin oxide films exhibiting normal and inclined columns. The porosity of tin oxide thin films was controlled by changing both the deposition flux of particles onto substrates and the sputtering pressure. To evaluate the influence of the porosity on the detection performances of these sensitive layers, benzene was chosen as pollutant gas. Among the numerous Volatile Organic Compounds (VOCs) that can be found in the air, BTEX compounds (*i.e.*, benzene, toluene, ethylbenzene, and xylenes) have long been known to severely threaten human health. Especially, benzene is considered as one of the most toxic compounds due to its carcinogenic effects even at very low concentrations, near the ppb level [25].

In this manuscript, SnO_2 thin films were thoroughly characterized in order to obtain information about texture, morphology and chemical composition. We used optical approaches to study the impact of deposition conditions on the films' porosity, inside the film and on the surface. Eventually, detection performances of the SnO_2-based gas sensors fabricated were evaluated in the presence of low concentrations of a representative aromatic indoor air pollutant, *i.e.*, benzene. In addition, we used Linear Discriminant Analysis (LDA) to evaluate the sensing performance of a system combining the responses of 4 nanostructured thin films sensitive surfaces for the discrimination of BTEX. Here, we have demonstrated the interest of using GLAD deposition technique and the role of sputtering pressure to obtain very porous sensitive thin films. In particular, we have discussed relationships between deposition parameters of tin oxide thin films and gas sensing performances.

2. Materials and Methods

2.1. Film growth

DC magnetron sputtering was used to deposit SnO_2 thin films in a 40 L homemade vacuum chamber at a base pressure below 10^{-8} mbar. Tin metallic target with a purity of 99.9 % and a diameter of 51 mm, was used. The distance between target and substrate was 65 mm and the current of the tin target (I_{Sn}) was fixed at 30 mA. During the magnetron sputtering deposition, oxygen to argon flow rate ratios were fixed at 0.6 and 0.8, leading to an argon sputtering pressures of 3.10^{-3} and 6.10^{-3} mbar, respectively. SnO_2 thin films were deposited onto glass and (100) silicon substrates as well as alumina sensor platforms at two different angles ($\alpha = 0°$ and 80° for normal and oblique films, respectively) and at two different argon sputtering pressures (3.10^{-3} and 6.10^{-3} mbar). A tilting angle of $\alpha = 80°$ was chosen based on previous studies [20,26] considering that films deposited at tilting angle $\alpha > 70°$ offered higher porosities compared to conventional sputtering angle. The deposition time was adjusted to get a film thickness close to 250 nm. The experimental setup used to deposit SnO_2 thin films can be found in previous works [26,27].

In this study, we labelled the nanostructured thin films "C" for normal angle ($\alpha = 0°$), while "I" was used for glancing angle films ($\alpha = 80°$). Additionally, the labels "3" and "6" were used for sputtering pressures of 3.10^{-3} and 6.10^{-3} mbar, respectively. For example, "I6" stands for an inclined film ($\alpha = 80°$) deposited at a sputtering pressure of 6.10^{-3} mbar.

2.2. Characterization

The surface and cross-section views of SnO_2 thin films were observed by scanning electron microscopy (SEM) in a Dual Beam SEM/FIB FEI Helios 600i microscope. Crystal structure of each film was characterized by X-ray diffraction (XRD) using a Bruker D8 focus diffractometer with a Cobalt X-ray tube (Co $\lambda K\alpha 1$ = 0.178897 nm) with a $\theta/2\theta$ configuration. Scans were performed with a step of 0.02° per 0.2s and a 2θ angle ranging from 20 to 80°. X-ray photoelectron spectroscopy (XPS) data were obtained with a PHI VersaProbe I system using a non-monochromatized Al Kα X-ray source ($h\upsilon$ = 1486.7 eV, power of 50 W). Energy calibrations were done on adventitious carbon (CC/CH bonds) at 248.8 eV. CasaXPS software was used for data treatment [28]. Optical transmission spectra of the thin film deposited on glass substrates were recorded with a Lambda 365 UV/Vis optical spectrometer. The reflectance and refractive index were determined using the Filmetrics F50 EXR reflectometer on the films deposited on (100) silicon substrates.

2.3. Sensing tests

For sensing tests, SnO_2 thin films were deposited onto 0.5 cm^2 alumina platforms (Heraeus MSP 632) equipped with interdigitated electrodes and allowed both the heating control and conductance measurement of the sensitive material as a function of time. Before exposure to pollutants, a conditioning sequence was applied to each sensor by aging the sensitive surface under a synthetic air flow (relative humidity (RH) 8% at 25°C, 100 mL min 1) at 500°C for 48 hours to ensure material crystallization. Concentrations of pollutants (BTEX) were obtained by adjusting the ratio between pollutant vapors and air. The normalized response of each sensor S was defined as S = (G-G°)/G°, where G and G° are the conductance under synthetic air mixed with BTEX and under pure synthetic air, respectively.

3. Results and Discussion

3.1. Morphology, structure and composition of the films

Figure 1 displays the different architectures obtained with the GLAD technique before and after a thermal treatment at 500 °C for 48 hours in ambient air. SnO_2 thin film deposited with a conventional incident angle (α = 0°) and under low argon sputtering pressure (3.10^{-3} mbar), *i.e.*, C3 film, exhibits a dense surface and a poorly defined cross-section morphology. On the other hand, for oblique films (α = 80°), the shadowing effect occurring during the early island nucleation on the surface causes voids formation between the small islands and subsequently creating columnar structures [29]. Films deposited at a higher pressure and / or with an angle of α = 80 ° exhibit an apparent more porous morphology. Basically, increasing the pressure in the deposition chamber induces multiple collisions in the gas phase, which makes it possible to cover areas which are not initially in the incident path of the sputtered particle flux. Thus, the surface becomes rougher with higher porosity. Despite a thermal treatment at 500 °C for several hours, the orientation of the nano-structured columns is preserved. In addition, it is worth noting that for I6 film, the columns tend to straighten out because of higher collisions due to higher pressure in the vacuum chamber and thus a less directional particle flux. The tilting angle of the columns for I3 and I6 films are 34° and 14°, respectively.

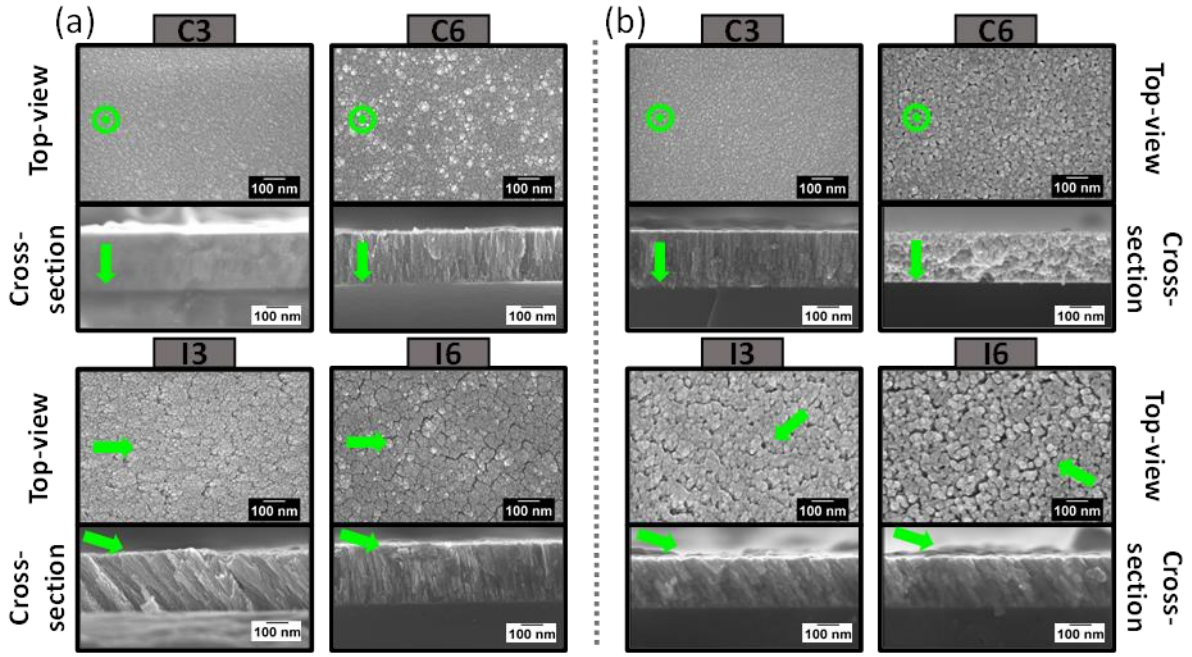

Figure 1. Top and cross-section views of SnO_2 thin films sputter-deposited on silicon (a) before and (b) after an annealing treatment in air for 48 hours at 500 °C. Arrows indicate the incoming particle flux during the deposition.

XRD patterns of the nano-structured SnO_2 thin films are shown in Figure 2 (a). As-deposited SnO_2 thin films with a pressure of 6.10^{-3} mbar remain amorphous, whatever the incidence angle (C6 and I6 thin films). Very weak peaks appear after an annealing treatment of 350°C for 48 hours. In contrast, all films deposited with a lower pressure (3.10^{-3} mbar, *i.e.*, C3 and I3 thin films) exhibit diffracted signals prior to a post thermal treatment. After a thermal treatment of 500 °C for 48 hours, XRD peaks of all films become sharper and stronger, indicating a better crystallinity. XRD patterns exhibit peaks between 20 and 70° corresponding to the (110), (101), (200), (211), and (220) reflections, which are assigned to the standard rutile-like crystalline structure of SnO_2 (cassiterite, space group: P42/mnm, JCPDS file no. 41-1445). No peaks of impurities were observed meaning the high purity of the as-prepared SnO_2 thin films. The corresponding tetragonal lattice constants are reported in Table 1.

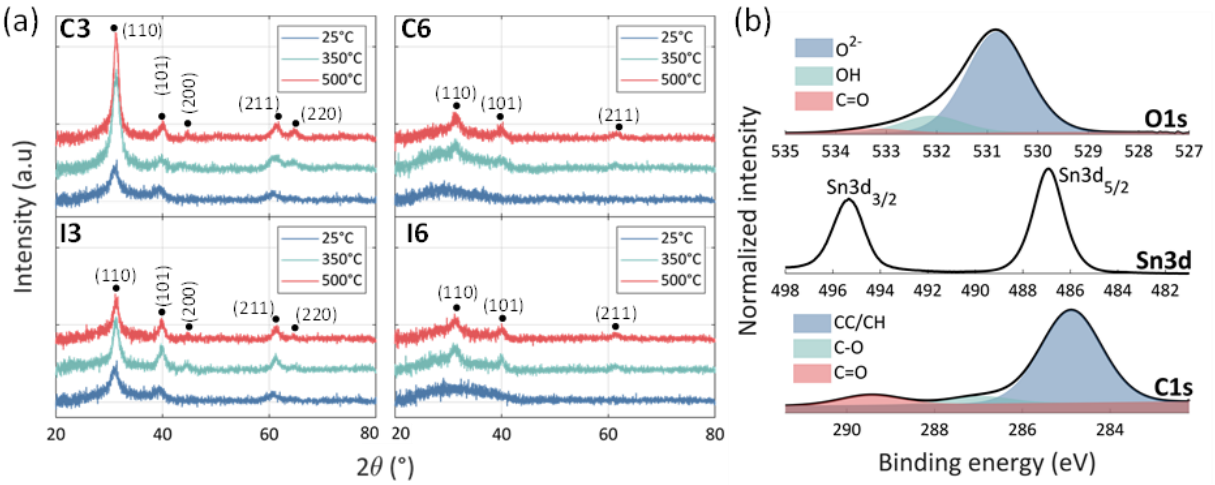

Figure 2. (a) XRD patterns of SnO_2 thin films sputter-deposited on glass substrates before and after an annealing treatment in ambient air for 48 hours at 2 different temperatures (350 and 500 °C). (b) XPS O1s, Sn3d and C1s spectral windows of the I6 SnO_2 thin film sputter-deposited on (100) Si substrate after an annealing treatment in ambient air at 500 °C for 48 hours.

Despite a slight evolution of the lattice constants with annealing temperature, these data agree with values already reported for SnO_2 (a = b = 4.737 Å and c = 3.186 Å) [30].

In addition, the average crystallite size of SnO_2 films was also calculated using the Scherrer's formula and the Williamson-Hall method (see Table 1) [31]. For both methods, the results show that the crystallite size increases with the annealing temperature and films deposited with a pressure of 6.10^{-3} mbar exhibit the lower crystallite size after a thermal treatment at 500°C, *i.e.*, 1.7 and 1.4 ± 0. 1 nm for C6 and I6 thin films, respectively.

Table 1. Crystallographic properties, surface chemical composition and porosity data of SnO_2 thin film.

		Lattice parameters (± 0.003 Å)		Average crystallite size (± 0. 1 nm)		Surface concentration (± 0.5 at. %)		Refractive index at 470 nm (± 0.01)	Packing density (± 2%)
		a = b	c	Scherrer	Williamson-Hall	O	Sn		
	25 °C	4.783	3.217	3.0	2.8	-	-	1.97	100
C3	350 °C	4.780	3.217	4.8	4.6	-	-	1.91	97
	500 °C	4.761	3.186	6.9	6.7	71.1	28.9	1.81	93
	25 °C	-	-	-	-	-	-	1.91	-
C6	350 °C	-	-	-	-	-	-	1.93	-
	500 °C	4.782	3.189	1.7	1.3	67.6	32.4	1.85	92
	25 °C	4.774	3.203	4.6	5.1	-	-	1.91	97
I3	350 °C	4.766	3.196	5.6	5.7	-	-	1.89	95
	500 °C	4.756	3.191	5.4	5.1	67.3	32.7	1.83	91
	25 °C	-	-	-	-	-	-	1.80	-
I6	350 °C	4.766	3.190	-	-	-	-	1.79	89
	500 °C	4.749	3.192	1.4	1.4	67.6	32.4	1.73	84

The surface chemistry of SnO_2 thin films deposited on (100) Si substrates was also investigated by XPS after a thermal treatment at 500 °C for 48 hours in ambient air. All XPS spectra showed the presence of oxygen, tin and carbon. A similar surface chemistry was observed for all films (see Figure S1 (a) in the Supplementary Materials file). Figure 2 (b) presents an example of the Sn3d, O1s and C1s core lines decomposition obtained from the I6 thin film sample. The evident contribution of the XPS C1s peak is attributed to the carbon contamination adsorbed on the surface of the films from the ambient air and during the annealing treatment. The decomposition of the O1s confirmed that it is built-up essentially as a mixture of three components. The main component at 530.81 eV is related to $O\text{-}Sn^{2+}$ and $O\text{-}Sn^{4+}$ bindings. Two additional components can be noticed at a binding energy of 533.22 and 532.09 eV corresponding to O=C and -O-H bindings, respectively. These species at the near-surface of SnO_2 materials and after exposure to air come from partially ionized –OH groups originating from dissociated atmospheric water and adsorbed CO/CO_2 from the ambient air [32]. The XPS Sn3d spectral line is narrow and symmetrical. The difference between binding energy of 3d5/2 level for SnO and SnO_2 is very low (486.6 and 486.9 eV, respectively) but, for all samples, the shape of the MNN Auger transition for Sn is close to that observed for SnO_2 (see Figure S1 (b)) [33]. It is worth noting that there is no contribution of metallic Sn (Sn^0) at the binding energy about 485 eV. This finding indicates that all films were completely oxidized after a thermal treatment at 500 °C in ambient air for 48 hours.

The relative surface concentrations of Sn and O, expressed in at. %, agree with the formula of SnO_2 composition (see Table 1). It is worth noting that the oxygen concentration is probably slightly overestimated due to the presence of contaminants at the near surface of the films.

3.2. Film growth

In this section, we present results concerning the influence of experimental deposition conditions on the porosity of SnO_2 thin films, through the films and on their surface.

3.2.1. Through the films

Figure 3 (a) shows the transmittance and reflectance spectra of films deposited on glass and (100) Si substrates, respectively, before and after an annealing treatment at 350 and 500°C for 48 hours. All films show a sharp absorption around 300 nm and exhibit a high transmission in the visible and near infrared region. Films deposited at 3.10^{-3} mbar (C3 and I3) show distinct interference fringes patterns in the optical transmittance spectra indicating homogeneous growth. On the other hand, films deposited at 6.10^{-3} mbar (C6 and I6) show minor interference fringes indicating inhomogeneity in the films. As mentioned in work of Ohlídal *et al.* [34], this inhomogeneity is due to surficial and inner roughness of the films. From Figure 3 (a), it can be underlined that there is no absorption edge shift for the C3 film whatever the annealing temperature. This indicates that there is less defects in C3 thin film in comparison with other films. The absence of interference fringes makes the determination of refractive indices from methods based on the adjustment of envelopes impossible [35].

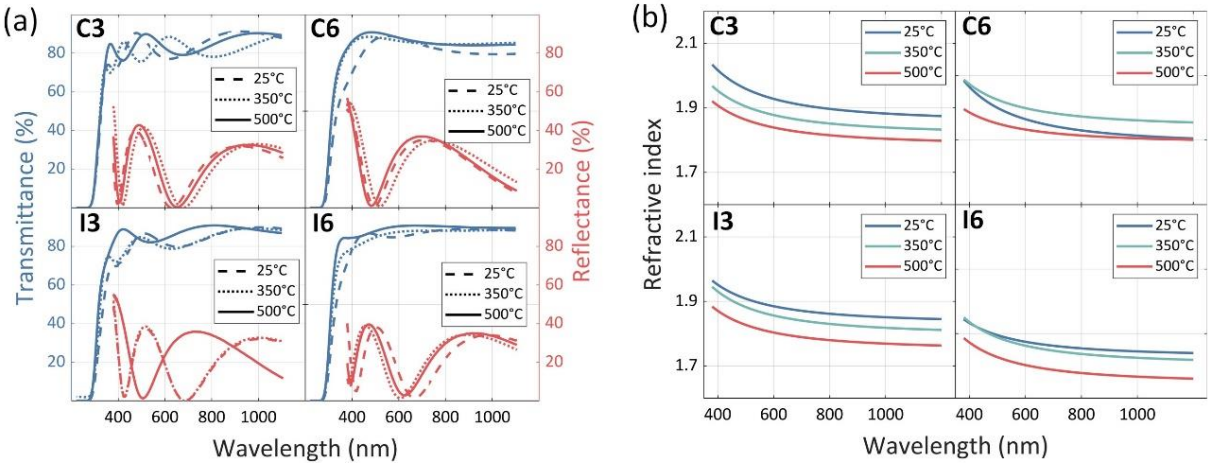

Figure 3. (a) Transmittance and reflectance spectra of SnO_2 thin films sputter-deposited on glass and (100) Si substrates before and after an annealing treatment in air for 48 hours and at 2 different temperatures (350 and 500 °C). (b) Evolution of the calculated refractive index *vs.* wavelength for all films at various temperatures.

Consequently, using the three phase Cauchy dispersion model (k = 0) showed in eq. 1, refractive indices can be calculated from the measured reflectance spectra (see again Fig. 3 (a)) [36].

$$n(\lambda) = A + \frac{B}{\lambda^2} + \frac{C}{\lambda^4} \quad (1)$$

Fitting constants A, B and C were calculated from the transmittance spectrum of C3 film and are estimated at 1.592, $7.44.10^4$ nm² and - $4.558.10^9$ nm⁴, respectively. These fitting constants were used for the determination of the refractive indices for all films.

Figure 3 (b) shows the evolution of the refractive indices as a function of the wavelength for each thin film, before and after the annealing treatment. The values of the refractive indices at 470 nm for all films annealed at every temperature are reported in Table 1. It is worth noting that these values were found to be lower than the corresponding value for bulk tin oxide at λ = 470 nm (n = 2 for bulk SnO_2 [37]). The refractive index was found to be lower for inclined columns (α = 80°) and for films deposited at high pressure (6.10^{-3}

mbar), which indicates higher porosity present inside these films [38]. In addition, after a thermal treatment, the value of the refractive index decreases for all films, indicating that the porosity of the films evolves with the annealing temperature. From the determined refractive indices at 470 nm and lattice constants previously calculated from XRD results (see Table 1), the packing density p was evaluated for all SnO_2 thin films using eq. 2 [39]. The calculated values are gathered in Table 1.

$$n_f = \frac{(1-p)n_v^2+(1+p)n_v^4 n_b^2}{(1+p)n_v^2+(1-p)n_b^2} + \frac{5}{2}\left(\frac{n_b^2-1}{n_b C_b}\right)(C_b - C_f) \quad (2)$$

n_f is the film refractive index at 470 nm, n_b the refractive index of bulk SnO_2 ($n_b = 2$), n_v the refractive index of void ($n_v = 1$), C_b the lattice parameter for bulk SnO_2 ($C_b = 3.186$ Å), C_f the lattice parameter for porous SnO_2, and p the packing density of the film.

For all studied films, the packing density p decreases with the annealing temperature which indicates an increase of the porosity inside the films. The evolution of the packing density is in line with the tendencies observed for the refractive index, *i.e.*, the inner porosity gradually rises between normal and inclined columns. The values of the inner porosities obtained in this work are in agreement with those found in the study of Bagga *et al.* [40], where the porosity of nanostructured SnO_2 thin films varied from 23% to 9%. Moreover, the porosity is favored with a higher deposition pressure, whatever the films deposited (normal or inclined columns). For example, the packing index is estimated to be around 91% (*i.e.* 9% inner porosity) for the inclined columns deposited at 3.10^{-3} mbar compared to 84% (*i.e.* 16% inner porosity) for the same structure at 6.10^{-3} mbar.

3.2.3. Surface porosity

Gas sensing being surface state dependent, the surface porosity of each thin film was also investigated using SEM images. Pore characterization including surface porosity and pore size distribution of each film was evaluated after a post treatment of binary SEM images using both ImageJ and MATLAB software. Figure 4 depicts for each thin film, the surface porosity determined by ImageJ versus the annealing temperature. The inserts show examples of the binary images obtained after the post image treatment for the I6 film, as-deposited and after two different annealing temperatures for 48 hours (350 and 500°C).

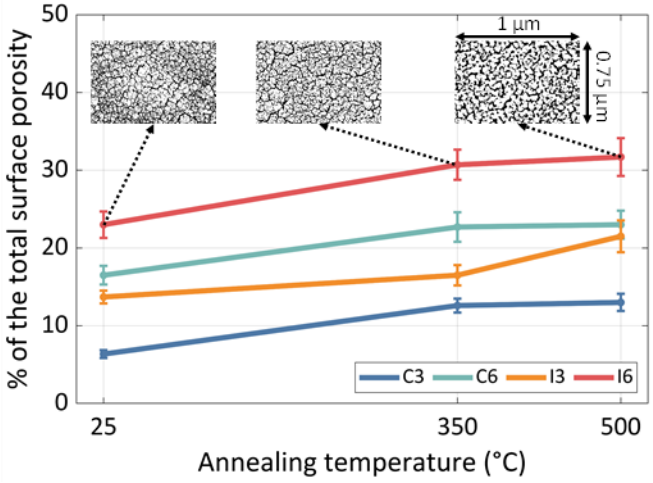

Figure 4. % of the total surface porosity *vs.* annealing temperature. The inserts show binary SEM images for I6 films (analyzed surface around 0.75 µm²).

For all films, the analyzed surface was around 0.75 µm², which constitutes a good representation of the total surface. A comparison between all films as deposited and whatever the annealing temperature, shows that by increasing the deposition pressure and tilting the substrate holder, the surface porosity increases significantly. To summarize, the

surface porosity increases according to the series: C3 < I3 < C6 < I6. By annealing the films at 500°C, with an intermediate temperature at 350°C, the growth of crystallites causes tensile stress which creates a more porous surface. Moreover, many studies showed that the annealing procedure increases the length and width of already existing pores. They become interconnected and form bigger pores that affect the surface morphology massively [41,42]. In addition, the cooling phase occurring when the temperature drops from 500 to 25°C in a short time (a few minutes), induces supplementary strain due to the mismatch of the expansion coefficients between the film and the substrate leading to the formation of additional cracks on the surface [43].

The pore size distribution (PSD) was also investigated using Otsu's method. This algorithm allows automatic multi-level thresholding of binarized SEM images. The pore segmentation was then obtained based on the lowest standard deviation of intensity in each segment. In addition, we used the MATLAB code developed by Rabbani *et al.* to determine the pore sizes [44]. This code was adapted to our analysis by adjusting the different parameters used for the thresholding method. Figure 5 (a) displays an example of the PSD and the corresponding boxplot showing the interquartile range median, minimum and maximum for the I6 thin film annealed at 500°C for 48 hours in ambient air.

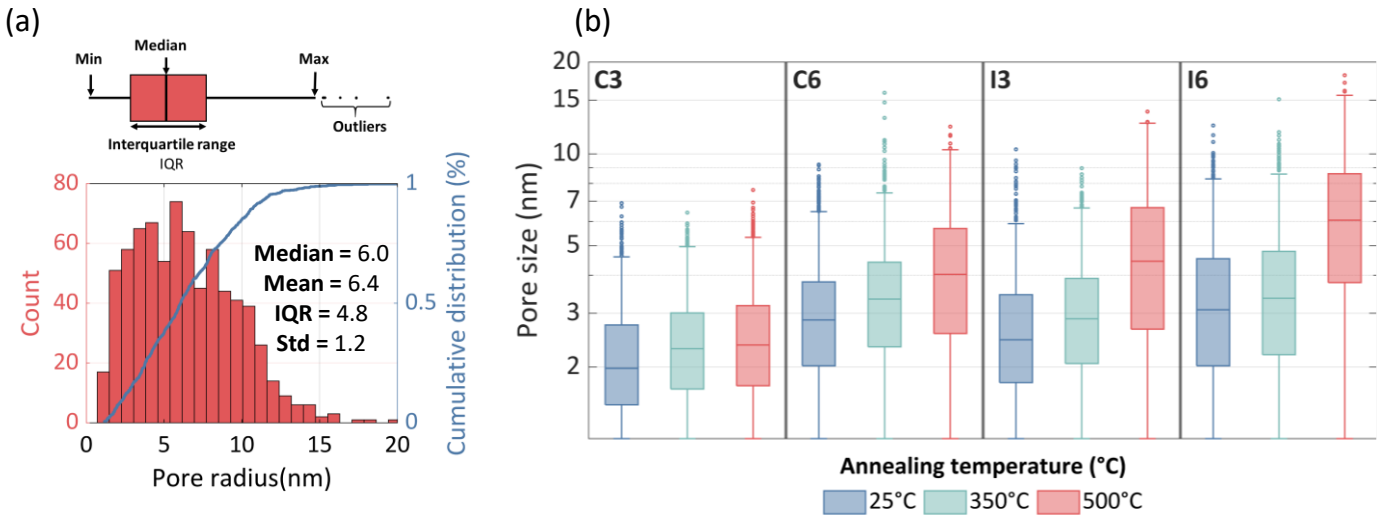

Figure 5. (a) Pore size distribution and boxplot calculated for the I6 film annealed at 500°C. (b) Boxplots showing the evolution of the pore size for all SnO_2 thin films sputter-deposited before and after an annealing treatment in air for 48 hours and at 2 different temperatures (350 and 500 °C).

The pore size distribution of I6 exhibits a multimodal distribution extending from *ca.* 1 to 20 nm, with the majority of the pores being in the mesopore range (*i.e.* width > 2 nm). Fig. S2 demonstrates that the PSDs of all films are right-skewed, regardless of the deposition conditions and the annealing temperature. After a thermal treatment at 500°C for 48 hours, C6, I3 and I6 films exhibit multimodal distributions indicating wider pore formation in the mesopore range. On the contrary, irrespective of the annealing treatment, C3 film presents a narrow unimodal PSD with the larger pores being less than 7 nm. Figure 5 (b) summarizes the corresponding boxplots calculated from the PSDs of all films. It was noticed that the pore size median increases continuously with the annealing temperature, especially for oblique films. This rise is noticeably higher for I6 film, with a pore size median going from 3.4 nm to 6.0 nm at 350°C and 500°C, respectively.

This porosity assessment shows that a simple study of the total surface porosity can be misleading as in some cases the porosity consists mostly of small and non-accessible pores. By combining the porosity results obtained from the inner and surface characterization, we obtained a better understanding of the evolution of the morphology of each tin

oxide thin film. Comparatively, I6 thin film annealed at 500°C offers the highest inner porosity (16%) and surface porosity (around 31%) and also a wide range of pore sizes [1-20 nm]. These textural properties prove to be of great interest for gas sensing applications since the diffusion of pollutants inside the material will be favored. It should be noted that the growth of the nano-structured columns, which is correlated to the porous structure of the films, is preserved regardless of the substrate used (Si, glass or alumina platforms).

After having evaluated the porous structure of the films, gas sensing performances were investigated.

3.3. Sensing performances

3.2.1. Benzene detection

The gas sensing properties of metal oxide-based gas sensors are highly affected by the operating temperature which generally ranging from 300 to 500°C. Figure S3 represents the typical electrical responses of the 4 sensors at various sensing temperatures and under 900 ppb of benzene for 2 min. Each benzene exposition was replicated 3 times. Figure 6 (a) displays the evolution of the relative conductance versus the sensitive surface temperature for each gas sensor (under 900 ppb of benzene for 2 min).

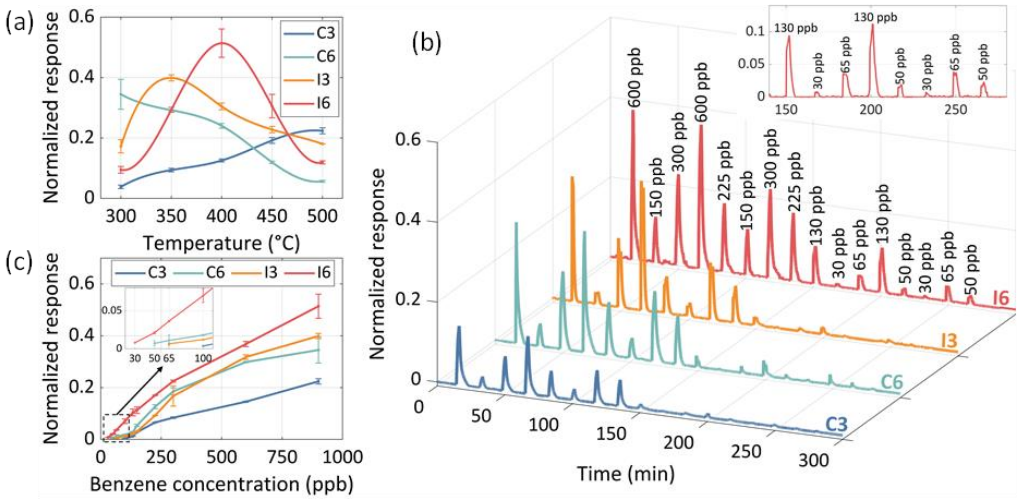

Figure 6. (a) Evolution of the normalized response as a function of the sensitive surface temperature for each gas sensor under 900 ppb of benzene. (b) Real-time response of each gas sensor for various benzene concentrations (sensing temperatures equal to 500, 300, 350 and 400 °C for C3, C6, I3 and I6 sensors, respectively). (c) Normalized response of the SnO_2-based gas sensors as a function of the benzene concentration. For all tests, 2 min. exposition time, 15 min. recovery time and 100 mL min^{-1} flow rate were applied.

It is evident that I6-based gas sensor showed a substantial change in the response as a function of metal oxide temperature. The optimized temperatures, corresponding to the sensor's temperature showing a maximal conductance under pollutant, were estimated at 500, 300, 350 and 400 °C for C3, C6, I3 and I6 sensors, respectively.

The detection mechanism of benzene with SnO_2-based gas sensors can be explained by considering that the chemisorbed oxygen species in the form O^- and O^{2-} are dominating for sensing layer's temperature above 200°C [45]. Since SnO_2 is an n-type semiconductor, and benzene a reducing compound, an oxidation mechanism of benzene molecules occurs at the sensor surface according to the successive reactions [46]:

$$C_6H_{6\,(gas)} \leftrightarrow C_6H_{6\,(ads)} \quad (3)$$

$$C_6H_{6\,(ads)} + 15\,O^-_{(ads)} \rightarrow 6\,CO_{2(gas)} + 3\,H_2O_{(gas)} + 15\,e^-_{c.b.} \quad (4)$$

$$C_6H_{6\,(ads)} + 15\,O^{2-}_{(ads)} \rightarrow 6\,CO_{2(gas)} + 3\,H_2O_{(gas)} + 30\,e^-_{c.b.} \quad (5)$$

c.b. is the conduction band of the material.

These reactions explain the increase of the conductance when SnO_2 is in contact with benzene. Figure 6 (b) plots the impulse response/recovery curves of each sensor at their respective optimized temperature for various concentrations of benzene mixed in air. The insert shows a zoom of the impulse response/recovery curves for I6 sensor at very low benzene concentrations. The sensors were stabilized in nearly dry air (8% RH at 25 °C) for 15 min. and then exposed to different benzene concentrations for 2 min. Each benzene concentration was chosen randomly and replicated twice in order to evaluate both the repeatability and the stability of each sensor. From Figure 6 (b), it can be easily found that there is a good correspondence between benzene concentrations and the dynamic response of each sensor. All sensors present an excellent repeatability and stability over time since the amplitude of the responses is in line with the benzene concentrations. The corresponding responses calculated from the change of the conductance of each sensor as a function of the benzene concentration are plotted in Figure 6 (c). It can be noticed that the I6 sensor exhibits the highest response in comparison with the other ones. Even though the difference in the deposition conditions (incidence angle and argon sputtering pressure), C6 and I3 sensors show similar responses to benzene.

The limit of detection (LOD), was defined by the concentration at which the amplitude of the signal was three times higher than the signal/noise ratio ($S = 0.002/N > 3$). For benzene, the LOD was estimated at 100 ppb for C3, 65 ppb for I3 and 50 ppb for C6 sensors while the LOD achieved for I6 sensor was around 30 ppb. From these results, it is interesting to note that not only the architecture of the film but also the deposition pressure are directly connected to the sensing performances. According to results obtained on the morphology and structure of the synthesized materials, the good sensing performances of I6 coating is mainly due to the high inner and surface porosity, the wide range of pore sizes and also to the small crystallites size (1.4 nm). The sensitivity of MOS gas sensors increases when the crystallite size is less than the double of the thickness of the space-charge layer (L) produced around the surface of the crystallites due to the chemisorbed oxygens. For SnO_2-based material, it is admitted that the space-charge layer L is equal to 3 nm [47]. In the present study, the average crystallite size obtained by XRD for all annealed thin films is lower than 2L and more particularly for the I6 sensitive surface the crystallite size is far lower.

3.2.3. BTEX discrimination

Since benzene is not the only air pollutant, we also studied the cross sensitivity of sensors for various VOCs (*i.e.*, toluene, ethylbenzene, ortho and para-xylene). Figure 7 (a) depicts the normalized responses of each sensor to around 100 ppb of each compound diluted in air and analyzed separately (*i.e.*, not in a mixture).

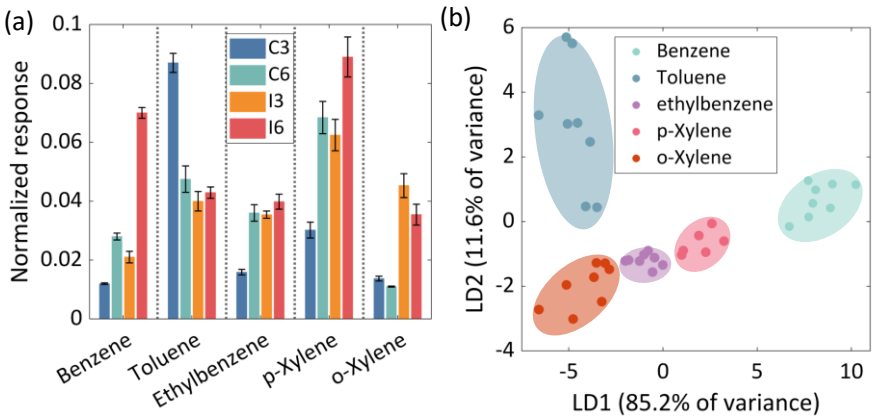

Figure 7. (a) Sensors response to various BTEX at a concentration of 100 ppb. (b) Linear Discriminant Analysis (LDA) scores using responses of the 4 SnO_2-based gas sensors. For all tests, 2 min. exposition time, 15 min. recovery time and 100 mL min^{-1} flow rate were applied.

For these experiments, sensing temperatures were maintained to 500, 300, 350 and 400 °C for C3, C6, I3 and I6 sensors, respectively. As expected, manufactured sensors are sensitive to all VOCs as long as each compound can react with the sensitive surface according to the following redox reactions:

$$C_xH_{y\,(gas)} \leftrightarrow C_xH_{y\,(ads)} \quad (6)$$

$$C_xH_{y\,(ads)} + \left(2x + \frac{y}{2}\right)O^{-}_{(ads)} \rightarrow x\,CO_{2(gas)} + \frac{y}{2}\,H_2O_{(gas)} + \left(2x + \frac{y}{2}\right)e^{-}_{c.b.} \quad (7)$$

$$C_xH_{y\,(ads)} + \left(2x + \frac{y}{2}\right)O^{2-}_{(ads)} \rightarrow x\,CO_{2(gas)} + \frac{y}{2}\,H_2O_{(gas)} + (4x + y)\,e^{-}_{c.b.} \quad (8)$$

In other words, this confirms that metal oxide-based gas sensors are not selective and it is not possible to identify one chemical compound in a mixture using a single gas sensor.

Nevertheless, classifying the species can be achieved by using a Linear Discriminant Analysis (LDA) that can map multi-dimensional data onto two- or three-dimensional axes [48]. This method uses linear combinations of sensors response to predict the class of a given observation (chemical nature of compound). In order to obtain greater precision on the discrimination of these VOCs compounds, we combined the normalized response and sensing kinetics (response and recovery times) of each sensor (*i.e.*, C3, C6, I3, and I6) after exposition to VOCs (Figure S4). Figure 7 (b) represents the LDA scores using the experimental data measured using the responses of the 4 sensors manufactured in this study and under BTEX. Plots confirm the ability to cluster points according to the chemical nature of species. The within-class distance of each VOC compound class in LDA are well gathered. This indicates that combining sensing responses of 4 gas sensors improves the discrimination of BTEX with concentrations ranging from 50 to 900 ppb.

Table 2 reports some literature data on the gas sensing performances of various metal oxide-based gas sensor arrays towards BTEX detection in synthetic air.

Table 2. A comparison of MOS based-gas sensor arrays for the detection of BTEX in air.

Materials	Number of sensors used	BTEX concentrations tested	Ref.
SnO_2	4	50 - 900 ppb (BTEX)	This study
NiO, WO_3, SnO_2	3	30-80 ppm (BTX)	[49]
SnO_2 NPs/cobalt-porphyrin, SnO_2 NPs/zinc-porphyrin, SnO_2 NPs/nickel-porphyrin and ZnO NPs/cobalt-porphyrin	4	1 – 9 ppm (BTEX)	[50]
SnO_2 with several additives, including Pt, Pd, CuO,LaO , ScO , TiO , WO or ZnO	10	benzene 50 ppm toluene 500 ppm	[51]

It should be also kept in mind that all results were obtained by analyzing compounds separately and in nearly dry air. By combining the responses from the 4 sensors fabricated in the present work, we obtain better sensing performances compared to those reported in the literature. It is worth noting that all sensor arrays reported in Table 2 are composed of several sensitive layers made with different doped or undoped materials (SnO_2, WO_3 …). The use of sensitive layers made of various materials makes it difficult to manufacture sensor arrays. Furthermore, the limit of detection of these arrays is around a few ppm which is much higher than the concentrations of BTEX found in air (a few ppb). In our

study, we showed that by modifying only the deposition conditions of the films (sputtering pressure and deposition angle) it is possible to obtain an efficient sensor array made of the same sensitive material (undoped SnO_2 here) for the discrimination of BTEX even at low concentrations (50 ppb). Consequently, this leads to an easier manufacturing procedure.

5. Conclusions

In this study, we used conventional and GLancing Angle Deposition (GLAD) reactive sputtering method to prepare nano-structured tin oxide-based sensitive films for gas sensor applications. The effect of the deposition parameters of SnO_2 films was studied in detail and it was found that the inter granular porosity can be tuned by adjusting the pressure and deposition angle. All sensors exhibited excellent stability and repeatability to benzene at a concentration of 900 ppb. The excellent sensing performances of the I6 sensor (deposition angle of 80° with a sputtering pressure of 6.10^{-3} mbar) were mainly attributed to the high inner and surface porosity (16 and 31 %, respectively), a wide range of pore sizes [1-20 nm], as well as to the small crystallite size (1.4 nm). With this deposition conditions, it is possible to reach a limit of detection close to 30 ppb with an operating temperature of 400°C. Despite the lack of intrinsic selectivity of each gas sensor taken individually, a chemical signature was obtained for the discrimination of a BTEX mixture by collectively considering the gas sensing responses from the 4 gas sensors developed in this study. We showed that it is possible to obtain a sensor array by using diverse undoped nano-structured SnO_2 sensitive films. In summary, the GLAD method seems to be very promising for the development of gas sensor array and has a great potential for exploring high-performance gas sensors for VOC detection.

Supplementary Materials: The following supporting information can be downloaded at: www.mdpi.com/xxx/s1, Figure S1: (a) XPS O1s, Sn3d and C1s spectral windows of the C3, C6 and I3 SnO_2 thin films and (b) experimental Sn MNN Auger spectra for C3, C6, I3 and I6 SnO_2 thin films SnO2 thin film. All films were sputter-deposited on (110) Si substrates and annealed in ambient air at 500 °C for 48 hours; Figure S2: Pore size distributions (PSDs) of all films sputter-deposited on (100) Si substrates, before and after annealing treatments at 350 and 500°C for 48 hours in ambient air. All PSDs were calculated using MATLAB software; Figure S3: Dynamic normalized response of the SnO_2-based gas sensors (C3, C6, I3 and I6) as a function of the sensing temperature under 900 ppb of benzene. For all tests, 2 min. exposition time, 15 min. recovery time and 100 mL min^{-1} flow rate were applied. Each benzene exposition was replicated 3 times; Figure S4: Dynamic normalized response of the SnO_2-based gas sensors (C3, C6, I3 and I6) for different concentrations of (a) toluene (b) ethylbenzene (c) p-xylene and (d) o-xylene. For all tests, 2 min. exposition time, 15 min. recovery time and 100 mL min^{-1} flow rate were applied.

Author Contributions: Investigation, methodology, data curation, software, A.E.M; Investigation, M.A.P.Y., A.K., O.H.; Formal analysis, validation, N.M.; Resources, F.B.; Funding acquisition, supervision, conceptualization, writing—review and editing, J.B.S. All authors have read and agreed to the published version of the manuscript.

Funding: This research was funded by Bourgogne Franche-Comté Region, the European fund FEDER, and the EUR EIPHI (contract ANR-17-EURE-0002) through the project DECOLAIR.

Data Availability Statement: Not applicable.

Acknowledgments: The authors would like to express their gratitude to the Bourgogne Franche-Comté Region, the European fund FEDER, and the EUR EIPHI (contract ANR-17-EURE-0002) for financial support through the project DECOLAIR. This work was partially supported by the French RENATECH network and its FEMTO-ST technological facility.

Conflicts of Interest: The authors declare no conflict of interest.

References

1. Spinelle, L.; Gerboles, M.; Kok, G.; Persijn, S.; Sauerwald, T. Review of Portable and Low-Cost Sensors for the Ambient Air Monitoring of Benzene and Other Volatile Organic Compounds. *Sensors* **2017**, *17*, 1520, doi:10.3390/s17071520.
2. Dhall, S.; Mehta, B.R.; Tyagi, A.K.; Sood, K. A Review on Environmental Gas Sensors: Materials and Technologies. *Sens. Int.* **2021**, *2*, 100116, doi:10.1016/j.sintl.2021.100116.
3. Shimizu, Y.; Jono, A.; Hyodo, T.; Egashira, M. Preparation of Large Mesoporous SnO2 Powder for Gas Sensor Application. *Sens. Actuators B Chem.* **2005**, *108*, 56–61, doi:10.1016/j.snb.2004.10.047.
4. Korotcenkov, G.; Han, S.-D.; Cho, B.K.; Brinzari, V. Grain Size Effects in Sensor Response of Nanostructured SnO2- and In2O3-Based Conductometric Thin Film Gas Sensor. *Crit. Rev. Solid State Mater. Sci.* **2009**, *34*, 1–17, doi:10.1080/10408430902815725.
5. Kong, Y.; Li, Y.; Cui, X.; Su, L.; Ma, D.; Lai, T.; Yao, L.; Xiao, X.; Wang, Y. SnO2 Nanostructured Materials Used as Gas Sensors for the Detection of Hazardous and Flammable Gases: A Review. *Nano Mater. Sci.* **2021**, doi:10.1016/j.nanoms.2021.05.006.
6. Sriram, S.R.; Parne, S.; Vaddadi, V.S.C.S.; Edla, D.; P., N.; Avala, R.R.; Yelsani, V.; Sontu, U.B. Nanostructured WO3 Based Gas Sensors: A Short Review. *Sens. Rev.* **2021**, *41*, 406–424, doi:10.1108/SR-05-2021-0153.
7. Pant, B.R.; Jayatissa, A.H. Gas Sensor Application of Zinc Oxide. In *Chemical Methods for Processing Nanomaterials*; CRC Press, 2021 ISBN 978-0-429-02318-7.
8. Tian, X.; Cui, X.; Lai, T.; Ren, J.; Yang, Z.; Xiao, M.; Wang, B.; Xiao, X.; Wang, Y. Gas Sensors Based on TiO2 Nanostructured Materials for the Detection of Hazardous Gases: A Review. *Nano Mater. Sci.* **2021**, doi:10.1016/j.nanoms.2021.05.011.
9. Seekaew, Y.; Wisitsoraat, A.; Phokharatkul, D.; Wongchoosuk, C. Room Temperature Toluene Gas Sensor Based on TiO2 Nanoparticles Decorated 3D Graphene-Carbon Nanotube Nanostructures. *Sens. Actuators B Chem.* **2019**, *279*, 69–78, doi:10.1016/j.snb.2018.09.095.
10. Subbiah, D.K.; Mani, G.K.; Babu, K.J.; Das, A.; Balaguru Rayappan, J.B. Nanostructured ZnO on Cotton Fabrics – A Novel Flexible Gas Sensor & UV Filter. *J. Clean. Prod.* **2018**, *194*, 372–382, doi:10.1016/j.jclepro.2018.05.110.
11. Nemec, P.; Hotový, I.; Andok, R.; Kostič, I. Increased Sensitivity of a Gas Sensor by Controlled Extension of TiO2 Active Area. *AIP Conf. Proc.* **2018**, *1996*, 020032, doi:10.1063/1.5048884.
12. Atanasova, G.; Dikovska, A.Og.; Dilova, T.; Georgieva, B.; Avdeev, G.V.; Stefanov, P.; Nedyalkov, N.N. Metal-Oxide Nanostructures Produced by PLD in Open Air for Gas Sensor Applications. *Appl. Surf. Sci.* **2019**, *470*, 861–869, doi:10.1016/j.apsusc.2018.11.178.
13. Singh, A.; Sharma, A.; Tomar, M.; Gupta, V. Tunable Nanostructured Columnar Growth of SnO2 for Efficient Detection of CO Gas. *Nanotechnology* **2018**, *29*, 065502, doi:10.1088/1361-6528/aa9bc0.
14. Nemec, P.; Hotovy, I.; Rehacek, V.; Andok, R. TiO2 Sensoric Structures with Controlled Extension of Their Active Area by Electron-Beam Lithography and Reactive Ion Etching Techniques. *AIP Conf. Proc.* **2021**, *2411*, 060003, doi:10.1063/5.0067745.
15. Bairagi, S.; Järrendahl, K.; Eriksson, F.; Hultman, L.; Birch, J.; Hsiao, C.-L. Glancing Angle Deposition and Growth Mechanism of Inclined AlN Nanostructures Using Reactive Magnetron Sputtering. *Coatings* **2020**, *10*, 768, doi:10.3390/coatings10080768.
16. El Beainou, R.; Garcia-Valenzuela, A.; Raschetti, M.; Cote, J.-M.; Alvarez, R.; Palmero, A.; Potin, V.; Martin, N. A 4-View Imaging to Reveal Microstructural Differences in Obliquely Sputter-Deposited Tungsten Films. *Mater. Lett.* **2020**, *264*, 127381, doi:10.1016/j.matlet.2020.127381.
17. Shin, S.J.; Bayu Aji, L.B.; Bae, J.H.; Engwall, A.M.; Nielsen, M.H.; Hammons, J.A.; Zuo, X.B.; Lee, B.; Lepro, X.; Mirkarimi, P.B.; et al. Oblique Angle Deposition of Boron Carbide Films by Magnetron Sputtering. *J. Appl. Phys.* **2021**, *130*, 125305, doi:10.1063/5.0056849.
18. Liedtke, S.; Grüner, C.; Lotnyk, A.; Rauschenbach, B. Glancing Angle Deposition of Sculptured Thin Metal Films at Room Temperature. *Nanotechnology* **2017**, *28*, 385604, doi:10.1088/1361-6528/aa7a79.

19. Pedrosa, P.; Ferreira, A.; Martin, N.; Yazdi, M.A.P.; Billard, A.; Lanceros-Méndez, S.; Vaz, F. Nano-Sculptured Janus-like TiAg Thin Films Obliquely Deposited by GLAD Co-Sputtering for Temperature Sensing. *Nanotechnology* **2018**, *29*, 355706, doi:10.1088/1361-6528/aacba8.
20. Sakkas, C.; Rauch, J.-Y.; Cote, J.-M.; Tissot, V.; Gavoille, J.; Martin, N. Tuning the Optical Properties of WO3 Films Exhibiting a Zigzag Columnar Microstructure. *Coatings* **2021**, *11*, 438, doi:10.3390/coatings11040438.
21. Rydosz, A.; Dyndał, K.; Andrysiewicz, W.; Grochala, D.; Marszałek, K. GLAD Magnetron Sputtered Ultra-Thin Copper Oxide Films for Gas-Sensing Application. *Coatings* **2020**, *10*, 378, doi:10.3390/coatings10040378.
22. Luo, P.; Xie, M.; Luo, J.; Kan, H.; Wei, Q. Nitric Oxide Sensors Using Nanospiral ZnO Thin Film Deposited by GLAD for Application to Exhaled Human Breath. *RSC Adv.* **2020**, *10*, 14877–14884, doi:10.1039/D0RA00488J.
23. Song, Y.G.; Shim, Y.-S.; Han, S.D.; Lee, H.R.; Ju, B.-K.; Kang, C.Y. Metal Oxide Nanocolumns for Extremely Sensitive Gas Sensors. *J. Sens. Sci. Technol.* **2016**, *25*, 184–188, doi:10.5369/JSST.2016.25.3.184.
24. Kang, M.; Cho, I.; Park, J.; Jeong, J.; Lee, K.; Lee, B.; Henriquez, D.D.O.; Yoon, K.; Park, I. High Accuracy Real-Time Multi-Gas Identification by a Batch-Uniform Gas Sensor Array and Deep Learning Algorithm. *ACS Sens.* **2022**, doi:10.1021/acssensors.1c01204.
25. Davidson, C.J.; Hannigan, J.H.; Bowen, S.E. Effects of Inhaled Combined Benzene, Toluene, Ethylbenzene, and Xylenes (BTEX): Toward an Environmental Exposure Model. *Environ. Toxicol. Pharmacol.* **2021**, *81*, 103518, doi:10.1016/j.etap.2020.103518.
26. Xu, X.; Arab Pour Yazdi, M.; Sanchez, J.-B.; Billard, A.; Berger, F.; Martin, N. Exploiting the Dodecane and Ozone Sensing Capabilities of Nanostructured Tungsten Oxide Films. *Sens. Actuators B Chem.* **2018**, *266*, 773–783, doi:10.1016/j.snb.2018.03.190.
27. Pedrosa, P.; Ferreira, A.; Cote, J.-M.; Martin, N.; Yazdi, M.A.P.; Billard, A.; Lanceros-Mendez, S.; Vaz, F. Influence of the Sputtering Pressure on the Morphological Features and Electrical Resistivity Anisotropy of Nanostructured Titanium Films. *Appl. Surf. Sci.* **2017**, *420*, 681–690, doi:10.1016/j.apsusc.2017.05.175.
28. Fairley, N.; Fernandez, V.; Richard-Plouet, M.; Guillot-Deudon, C.; Walton, J.; Smith, E.; Flahaut, D.; Greiner, M.; Biesinger, M.; Tougaard, S.; et al. Systematic and Collaborative Approach to Problem Solving Using X-Ray Photoelectron Spectroscopy. *Appl. Surf. Sci. Adv.* **2021**, *5*, 100112, doi:10.1016/j.apsadv.2021.100112.
29. Chen, L.-C.; Chen, C.-C.; Sung, Y.-T.; Hsu, Y.-Y. Oblique-Angle Sputtering Effects on Characteristics of Nanocolumnar Structure Anisotropic Indium Tin Oxide Films. *J. Electrochem. Soc.* **2009**, *156*, H471, doi:10.1149/1.3116248.
30. Bolzan, A.A.; Fong, C.; Kennedy, B.J.; Howard, C.J. Structural Studies of Rutile-Type Metal Dioxides. *Acta Crystallogr. B* **1997**, *53*, 373–380, doi:10.1107/S0108768197001468.
31. Mustapha, S.; Ndamitso, M.M.; Abdulkareem, A.S.; Tijani, J.O.; Shuaib, D.T.; Mohammed, A.K.; Sumaila, A. Comparative Study of Crystallite Size Using Williamson-Hall and Debye-Scherrer Plots for ZnO Nanoparticles. *Adv. Nat. Sci. Nanosci. Nanotechnol.* **2019**, *10*, 045013, doi:10.1088/2043-6254/ab52f7.
32. Güzelçimen, F.; Tanören, B.; Çetinkaya, Ç.; Kaya, M.D.; Efkere, H.İ.; Özen, Y.; Bingöl, D.; Sirkeci, M.; Kınacı, B.; Ünlü, M.B.; et al. The Effect of Thickness on Surface Structure of Rf Sputtered TiO2 Thin Films by XPS, SEM/EDS, AFM and SAM. *Vacuum* **2020**, *182*, 109766, doi:10.1016/j.vacuum.2020.109766.
33. Kövér, L.; Kovács, Zs.; Sanjinés, R.; Moretti, G.; Cserny, I.; Margaritondo, G.; Pálinkás, J.; Adachi, H. Electronic Structure of Tin Oxides: High-Resolution Study of XPS and Auger Spectra. *Surf. Interface Anal.* **1995**, *23*, 461–466, doi:10.1002/sia.740230705.
34. Ohlídal, I.; Vohánka, J.; Čermák, M. Optics of Inhomogeneous Thin Films with Defects: Application to Optical Characterization. *Coatings* **2020**, *11*, 22, doi:10.3390/coatings11010022.
35. Sánchez-González, J.; Díaz-Parralejo, A.; Ortiz, A.L.; Guiberteau, F. Determination of Optical Properties in Nanostructured Thin Films Using the Swanepoel Method. *Appl. Surf. Sci.* **2006**, *252*, 6013–6017, doi:10.1016/j.apsusc.2005.11.009.

36. Wang, Z.-Y.; Zhang, R.-J.; Lu, H.-L.; Chen, X.; Sun, Y.; Zhang, Y.; Wei, Y.-F.; Xu, J.-P.; Wang, S.-Y.; Zheng, Y.-X.; et al. The Impact of Thickness and Thermal Annealing on Refractive Index for Aluminum Oxide Thin Films Deposited by Atomic Layer Deposition. *Nanoscale Res. Lett.* **2015**, *10*, 46, doi:10.1186/s11671-015-0757-y.
37. Raoult, E.; Bodeux, R.; Jutteau, S.; Rives, S.; Yaiche, A.; Coutancier, D.; Rousset, J.; Collin, S. Optical characterizations and modelling of semitransparent perovskite solar cells for tandem applications. *36th European Photovoltaic Solar Energy Conference and Exhibition* **2019**, 757 - 763, doi: 10.4229/EUPVSEC20192019-3BV.2.53
38. Robbie, K.; Brett, M.J. Sculptured Thin Films and Glancing Angle Deposition: Growth Mechanics and Applications. *J. Vac. Sci. Technol. Vac. Surf. Films* **1997**, *15*, 1460–1465, doi:10.1116/1.580562.
39. Sharma, A.; Tomar, M.; Gupta, V. SnO2 Thin Film Sensor with Enhanced Response for NO_2 Gas at Lower Temperatures. *Sens. Actuators B Chem.* **2011**, *156*, 743–752, doi:10.1016/j.snb.2011.02.033.
40. Bagga, S.; Akhtar, J.; Mishra, S. Influence of Porosity on the Properties of Nanostructured Tin Oxide Thin Film. *Mater. Res. Express* **2018**, *5*, 116406, doi:10.1088/2053-1591/aadd40.
41. Tang, Z.; Chan, P.C.H.; Sharma, R.K.; Yan, G.; Hsing, I.-M.; Sin, J.K.O. Investigation and Control of Microcracks in Tin Oxide Gas Sensing Thin-Films. *Sens. Actuators B Chem.* **2001**, *79*, 39–47, doi:10.1016/S0925-4005(01)00846-2.
42. Sonder, E.; Levinson, L.M.; Katz, W. Role of Short-circuiting Pathways in Reduced ZnO Varistors. *J. Appl. Phys.* **1985**, *58*, 4420–4425, doi:10.1063/1.335533.
43. Filipovic, L.; Selberherr, S. Performance and Stress Analysis of Metal Oxide Films for CMOS-Integrated Gas Sensors. *Sensors* **2015**, *15*, 7206–7227, doi:10.3390/s150407206.
44. Rabbani, A.; Salehi, S. Dynamic Modeling of the Formation Damage and Mud Cake Deposition Using Filtration Theories Coupled with SEM Image Processing. *J. Nat. Gas Sci. Eng.* **2017**, *42*, 157–168, doi:10.1016/j.jngse.2017.02.047.
45. Kohl, D. Surface Processes in the Detection of Reducing Gases with SnO2-Based Devices. *Sens. Actuators* **1989**, *18*, 71–113, doi:10.1016/0250-6874(89)87026-X.
46. Mirzaei, A.; Kim, J.-H.; Kim, H.W.; Kim, S.S. Resistive-Based Gas Sensors for Detection of Benzene, Toluene and Xylene (BTX) Gases: A Review. *J. Mater. Chem. C* **2018**, *6*, 4342–4370, doi:10.1039/C8TC00245B.
47. Xu, C.; Tamaki, J.; Miura, N.; Yamazoe, N. Grain Size Effects on Gas Sensitivity of Porous SnO2-Based Elements. *Sens. Actuators B Chem.* **1991**, *3*, 147–155, doi:10.1016/0925-4005(91)80207-Z.
48. Akbar, M.A.; Ait Si Ali, A.; Amira, A.; Bensaali, F.; Benammar, M.; Hassan, M.; Bermak, A. An Empirical Study for PCA- and LDA-Based Feature Reduction for Gas Identification. *IEEE Sens. J.* **2016**, *16*, 5734–5746, doi:10.1109/JSEN.2016.2565721.
49. Liu, H.; Meng, G.; Deng, Z.; Nagashima, K.; Wang, S.; Dai, T.; Li, L.; Yanagida, T.; Fang, X. Discriminating BTX Molecules by the Nonselective Metal Oxide Sensor-Based Smart Sensing System. *ACS Sens.* **2021**, *6*, 4167–4175, doi:10.1021/acssensors.1c01704.
50. Cho, B.; Lee, K.; Pyo, S.; Kim, J. Fabrication and Characterization of VOC Sensor Array Based on SnO2 and ZnO Nanoparticles Functionalized by Metalloporphyrins. *Micro Nano Syst. Lett.* **2018**, *6*, 10, doi:10.1186/s40486-018-0072-3.
51. Lee, D.-S.; Kim, Y.T.; Huh, J.-S.; Lee, D.-D. Fabrication and Characteristics of SnO2 Gas Sensor Array for Volatile Organic Compounds Recognition. *Thin Solid Films* **2002**, *416*, 271–278, doi:10.1016/S0040-6090(02)00619-3.